



HAL
open science

Reproducibility in G_0W_0 calculations for solids

Tonatiuh Rangel, Mauro del Ben, Daniele Varsano, Gabriel Antonius, Fabien Bruneval, Felipe H. da Jornada, Michiel J. van Setten, Okan K. Orhan, David D. O'Regan, Andrew Canning, et al.

► To cite this version:

Tonatiuh Rangel, Mauro del Ben, Daniele Varsano, Gabriel Antonius, Fabien Bruneval, et al.. Reproducibility in G_0W_0 calculations for solids. Computer Physics Communications, 2020, 255, pp.107242. 10.1016/j.cpc.2020.107242 . cea-02927610

HAL Id: cea-02927610

<https://cea.hal.science/cea-02927610>

Submitted on 7 May 2021

HAL is a multi-disciplinary open access archive for the deposit and dissemination of scientific research documents, whether they are published or not. The documents may come from teaching and research institutions in France or abroad, or from public or private research centers.

L'archive ouverte pluridisciplinaire **HAL**, est destinée au dépôt et à la diffusion de documents scientifiques de niveau recherche, publiés ou non, émanant des établissements d'enseignement et de recherche français ou étrangers, des laboratoires publics ou privés.

Reproducibility in G_0W_0 Calculations for Solids

Tonatiuh Rangel,^{1,2,*} Mauro Del Ben,³ Daniele Varsano,^{4,5} Gabriel Antonius,^{2,6,7} Fabien Bruneval,^{8,1,6} Felipe H. da Jornada,^{2,6} Michiel J. van Setten,^{9,5,10} Okan K. Orhan,¹¹ David D. O'Regan,¹¹ Andrew Canning,³ Andrea Ferretti,^{4,5} Andrea Marini,^{12,5} Gian-Marco Rignanesi,^{9,5} Jack Deslippe,¹³ Steven G. Louie,^{2,6} and Jeffrey B. Neaton^{1,2,14,†}

¹*Molecular Foundry, Lawrence Berkeley National Laboratory, Berkeley, California 94720, United States*

²*Department of Physics, University of California at Berkeley, California 94720, United States*

³*Computational Research Division, Lawrence Berkeley National Laboratory, Berkeley, California 94720, United States*

⁴*Centro S3, CNR-Istituto Nanoscienze, I-41125 Modena, Italy*

⁵*European Theoretical Spectroscopy Facility (ETSF)*

⁶*Materials Sciences Division, Lawrence Berkeley National Laboratory, Berkeley, California 94720, United States*

⁷*Département de Chimie, Biochimie et Physique, Institut de recherche sur l'hydrogène, Université du Québec à Trois-Rivières, Qc, Canada*

⁸*DEN, Service de Recherches de Métallurgie Physique, Université Paris-Saclay, CEA, F-91191 Gif-sur-Yvette, France*

⁹*Institute of Condensed Matter and Nanoscience (IMCN), Université catholique de Louvain, 1348 Louvain-la-Neuve, Belgium*

¹⁰*IMEC, Kapeldreef 75, 3001 Leuven, Belgium*

¹¹*School of Physics, Trinity College Dublin, The University of Dublin, Dublin 2, Ireland*

¹²*Istituto di Struttura della Materia of the National Research Council, Via Salaria Km 29.3, I-00016 Montelibretti, Italy*

¹³*NERSC, Lawrence Berkeley National Laboratory, Berkeley, California 94720, United States*

¹⁴*Kavli Energy Nanosciences Institute at Berkeley, Berkeley, California 94720, United States*

Ab initio many-body perturbation theory within the GW approximation is a Green's function formalism widely used in the calculation of quasiparticle excitation energies of solids. In what has become an increasingly standard approach, Kohn-Sham eigenenergies, generated from a DFT calculation with a strategically-chosen exchange correlation functional “starting point”, are used to construct G and W , and then perturbatively corrected by the resultant GW self-energy. In practice, there are several ways to construct the GW self-energy, and these can lead to variations in predicted quasiparticle energies. For example, for ZnO and TiO₂, reported GW fundamental gaps can vary by more than 1 eV. In this work, we address the convergence and key approximations in contemporary G_0W_0 calculations, including frequency-integration schemes and the treatment of the Coulomb divergence in the exact-exchange term. We study several systems, and compare three different GW codes: BERKELEYGW, ABINIT and YAMBO. We demonstrate, for the first time, that the same quasiparticle energies for systems in the condensed phase can be obtained with different codes, and we provide a comprehensive assessment of implementations of the GW approximation.

I. INTRODUCTION

Quantitative prediction of charged single-particle excitations in otherwise interacting many-particle systems such as solids is a key component of the design and discovery of materials and the fundamental understanding of matter at the atomistic level. A rigorous formalism for computing such particle-like excitations is many-body perturbation theory, in which electron addition/removal energies are solutions to an effective non-Hermitian single-particle Hamiltonian with a non-local energy-dependent potential, or self-energy operator Σ . In the so-called GW method,¹ the self-energy Σ is approximated, to lowest order in the screened Coulomb interaction W , as iGW , where G is the one-electron Green's function. In a standard approach, G and W are constructed from a (either regular or generalized²) Kohn-Sham (KS) eigensystem, computed via density functional theory (DFT), and the KS eigenvalues are corrected perturbatively with a one-shot G_0W_0 self-energy, where the subscript indicates that G and W are not updated self-

consistently. By accounting for the screening of the crystal environment, GW is naturally applicable to solids and has proven quite effective in predicting quasiparticle energies of a wide range of crystals.³⁻⁸ However, because of the complexity, computational cost, and the number of convergence parameters involved, numerical approximations are required in GW calculations, and varying algorithms in different codes can sometimes yield distinct results.

Crystalline silicon is probably the most-studied test-bed solid for GW . Having high crystal symmetry and containing only sp -bonded orbitals, silicon is a relatively-simple system, for which GW within standard approximations yields accurate quasiparticle energies and sizable self-energy corrections.^{3,4} Transition metals (TMs) and transition metal oxides (TMOs), with localized d or f electrons, present a bigger numerical challenge for GW . When dealing with TMs, care should be taken in the technical details and approximations used within GW . For instance, the convergence criteria,⁹ and the choice of frequency-integration scheme¹⁰⁻¹⁴ and pseu-

dopotentials¹⁵ can yield substantially different results. Several *GW* works for rutile TiO₂ have reported gaps ranging from 3.1 to 4.8 eV,^{11,16–20} while for ZnO gaps published so far range from 2.6 to 4.5 eV.^{9,12,15,21–24} Thanks to advances in computational resources and algorithms, recent works have explored convergence beyond past limits,^{9,12,15,21,22,24} and accurate pseudopotentials specific for *GW* have been proposed,^{15,25} a general agreement on the *GW* quasiparticle energies with different codes has yet to be perceived as being achieved for the difficult cases. The growing popularity of *GW*, the multiple dedicated codes used for *GW*, and the existing challenges and discrepancies encountered when performing *GW* on increasingly chemically complex systems, such as TMs and TMOs, make it imperative to have reproducibility of predictions from different *GW* codes.

In this work, we report the results of a detailed comparison of three different plane-wave-based *GW* codes, and we find that predictions from these codes can agree very well, under given similarly physically sound approximations. For purposes of assessment, we study the representative solids Si, Au, TiO₂, and ZnO with the open-source *GW* codes ABINIT (ABI)²⁶, BERKELEYGW (BGW),²⁷ and YAMBO (YMB).²⁸ Our benchmark calculations provide a framework for users and developers to document the precision of new applications and methodological improvements, and provides standards for the reproducibility of *GW* calculations.

II. THE *GW* METHOD IN PRACTICE

The *GW* method is an interacting Green's function formalism which accounts for the response of the system to addition or removal of a single electron in an interacting *N*-electrons system, via a non-Hermitian, non-local, and frequency-dependent self-energy operator

$$\Sigma(\mathbf{r}, \mathbf{r}'; \omega) = \frac{i}{2\pi} \int d\omega' e^{i\omega'\eta} G(\mathbf{r}, \mathbf{r}'; \omega + \omega') W(\mathbf{r}, \mathbf{r}'; \omega'), \quad (1)$$

where η is a positive infinitesimal and the bare Coulomb potential v and the inverse of the dielectric matrix ϵ^{-1} are used to construct the screened Coulomb potential

$$W(\mathbf{r}, \mathbf{r}'; \omega) = \int d\mathbf{r}'' \epsilon^{-1}(\mathbf{r}, \mathbf{r}''; \omega) v(\mathbf{r}'', \mathbf{r}'). \quad (2)$$

In the so-called one-shot *GW*, also known as G_0W_0 , the quasiparticle energies E_i^{QP} are solved perturbatively from a mean-field Kohn-Sham (KS) starting point; that is, G_0 and W_0 are constructed from the KS mean-field. In this approach, which implicitly assumes the KS wavefunctions ψ_i^{KS} are close to the QP wavefunctions ψ_i^{QP} , the QP energy of the i th state is given by^{3,4}

$$E_i^{\text{QP}} = E_i^{\text{KS}} + \langle \psi_i^{\text{KS}} | \Sigma(E_i^{\text{QP}}) - V_{xc} | \psi_i^{\text{KS}} \rangle \quad (3)$$

where V_{xc} is the KS exchange-correlation potential, and Σ is evaluated at the QP energy E_i^{QP} . A common ap-

proximation is to linearize Σ in the QP energy with a first-order Taylor expansion around E_i^{KS} , such that

$$E_i^{\text{QP}} = E_i^{\text{KS}} + Z_i \langle \psi_i^{\text{KS}} | \Sigma(E_i^{\text{KS}}) - V_{xc} | \psi_i^{\text{KS}} \rangle, \quad (4)$$

with the renormalization factor

$$Z_i = \left[1 - \langle \psi_i^{\text{KS}} | \frac{\partial \Sigma(\omega)}{\partial \omega} \Big|_{\omega=E_i^{\text{KS}}} | \psi_i^{\text{KS}} \rangle \right]^{-1}. \quad (5)$$

As discussed later, the standard linearization scheme should be used with care as it can lead to relatively large deviations (up to 0.2 eV in ZnO) in predicted QP energies.

A source of deviation among *GW* results with different codes is the numerical integration scheme used to evaluate the *frequency dependence* of Σ in Eq. (1).^{10–13} A common practice to reduce computational cost is to approximate the dielectric function with a single-pole via a generalized plasmon-pole model (PPM). For each set of momentum components $(\mathbf{q}, \mathbf{G}, \mathbf{G}')$, the inverse dielectric function ϵ^{-1} in this approximation takes the form

$$\text{Im } \epsilon_{\mathbf{G}, \mathbf{G}'}^{-1}(\mathbf{q}, \omega) = A_{\mathbf{G}, \mathbf{G}'}(\mathbf{q}) \times [\delta(\omega - \tilde{\omega}_{\mathbf{G}, \mathbf{G}'}(\mathbf{q})) - \delta(\omega + \tilde{\omega}_{\mathbf{G}, \mathbf{G}'}(\mathbf{q}))] \quad (6)$$

$$\text{Re } \epsilon_{\mathbf{G}, \mathbf{G}'}^{-1}(\mathbf{q}, \omega) = 1 - \frac{A_{\mathbf{G}, \mathbf{G}'}(\mathbf{q}) \tilde{\omega}_{\mathbf{G}, \mathbf{G}'}^2(\mathbf{q})}{\omega^2 - \tilde{\omega}_{\mathbf{G}, \mathbf{G}'}^2(\mathbf{q})}, \quad (7)$$

where the matrices $A_{\mathbf{G}, \mathbf{G}'}(\mathbf{q})$ and $\tilde{\omega}_{\mathbf{G}, \mathbf{G}'}(\mathbf{q})$ are to be determined.⁴ In the Hybertsen-Louie (HL) approach, the PPM parameters are determined from sum rules and by evaluating the dielectric function at $\omega = 0$.⁴ In the Godby-Needs (GN) scheme, the parameters are set by calculating ϵ^{-1} at two frequencies: $\omega = 0$ and an imaginary frequency close to the plasma frequency.²⁹ Both ABINIT and YAMBO use the PPM-GN scheme as default; BERKELEYGW uses a PPM-HL version modified to deal with non-centrosymmetric systems.^{27,30} When calculating $\epsilon(\mathbf{q}, \mathbf{q}'; \omega = 0)$ to find the PPM-HL parameters from Eq. (7), it may happen that the dielectric function cannot be satisfactorily approximated by a single-pole model for certain $(\mathbf{q}, \mathbf{G}, \mathbf{G}')$ leading to imaginary frequencies $\omega_{\mathbf{G}, \mathbf{G}'}(\mathbf{q})$. Such modes, referred to here as *unfulfilled PPM modes* ω^{unf} , are neglected in the original version of the PPM-HL.⁴ Other treatments of the unfulfilled modes are also possible. For example, these frequencies can be given an arbitrary value of $\omega^{\text{unf}} = 1$ Ha, which was the default behavior in ABINIT and YAMBO.

Beyond PPMs, it is increasingly standard for *GW* codes to use *full-frequency* (FF) methods, in which the frequency convolution in Eq. (1) is evaluated numerically. A straightforward integration method on the real axis (FF-RA) is available in codes such as YAMBO and BERKELEYGW. However, such an integration of Σ in Eq. (1) presents numerical challenges since G and W possess poles close to the real axis. To avoid this difficulty, in the full-frequency *contour-deformation* (FF-CD) method, the integration contour in Eq. (1) is deformed

into the complex plane, into a region where the integrand is smooth; the alternative integration path must be supplemented with the residues from the poles of G , as explained in detail in Refs. 5, 31, and 32. The FF-CD method is available in ABINIT and has been recently implemented into BERKELEYGW.^{33,34} For other FF methods we refer the reader to Refs. 20, 35, and 36.

The self-energy is usually split into a frequency-independent exchange part Σ_x and a correlation part Σ_c , so that $\Sigma(\mathbf{r}, \mathbf{r}'; \omega) = \Sigma_x(\mathbf{r}, \mathbf{r}') + \Sigma_c(\mathbf{r}, \mathbf{r}'; \omega)$,³⁷ where the matrix element of Σ_x between two Bloch states reads:

$$\langle i\mathbf{k} | \Sigma_x | j\mathbf{k} \rangle = - \sum_{\mathbf{q}, \mathbf{G}} v(\mathbf{q} + \mathbf{G}) \mathcal{F}_{ij\mathbf{k}}(\mathbf{q} + \mathbf{G}) \quad (8)$$

and

$$\mathcal{F}_{ij\mathbf{k}}(\mathbf{q} + \mathbf{G}) = \sum_{v \in occ.} M_{iv\mathbf{k}}(\mathbf{q} + \mathbf{G}) M_{jv\mathbf{k}}^*(\mathbf{q} + \mathbf{G}). \quad (9)$$

Here, $M_{iv\mathbf{k}} = \langle i\mathbf{k} | e^{i(\mathbf{q} + \mathbf{G}) \cdot \mathbf{r}} | v\mathbf{k} - \mathbf{q} \rangle$ are matrix elements for states i and v at k-point \mathbf{k} . The expression for Σ_c is given in Ref. 12.

The exchange term, also present in the evaluation of Fock exchange for hybrid functionals in DFT, features a divergence in the Coulomb potential $v(\mathbf{q} + \mathbf{G}) = 4\pi e^2 / |\mathbf{q} + \mathbf{G}|^2$ as $\mathbf{q} \rightarrow 0$ for $\mathbf{G} = 0$. Several schemes have been proposed to treat the divergence of the Coulomb term.^{27,28,38-46} For instance, in the *spherical-cutoff* technique, the Coulomb interaction is attenuated beyond R_c and $v(0)$ is replaced with $2\pi e^2 R_c^2$, where the sphere of radius R_c has volume equal to that of the unit cell times the number of k-points.⁴⁴ In ABINIT by default the Coulomb singularity is approached by an auxiliary-function integration method detailed in Ref. 43. Other codes avoid the Coulomb singularity by replacing the value of $q \rightarrow 0$ in Eq. (8) by an integral around $q \simeq 0$.^{27,28,47} This method is applicable to any \mathbf{q} point in the BZ by assuming,

$$\langle i\mathbf{k} | \Sigma_x | j\mathbf{k} \rangle = - \sum_{\mathbf{q}, \mathbf{G}} \int_{R_{\mathbf{q}+\mathbf{G}}} \frac{d\mathbf{q}'}{\Omega(R_{\mathbf{q}+\mathbf{G}})} v(\mathbf{q} + \mathbf{q}' + \mathbf{G}) \times \mathcal{F}_{ij\mathbf{k}}(\mathbf{q} + \mathbf{G}), \quad (10)$$

where the integral is performed over the BZ region $R_{\mathbf{q}+\mathbf{G}}$, which is associated with a volume $\Omega(R_{\mathbf{q}+\mathbf{G}})$, and centered around each $\mathbf{q} + \mathbf{G}$ point. This method gives the effect of a larger sampling of points around \mathbf{q} assuming that $\mathcal{F}(\mathbf{q} + \mathbf{G})$ is constant over that region.

In the ‘‘random integration method’’ (RIM) implemented in YAMBO²⁸ and ‘‘Monte Carlo averaging’’ (MC average) technique used in BERKELEYGW²⁷ the integral is evaluated using a stochastic scheme. In both codes a stochastic scheme is also used to evaluate every term of the form $\int d^m \mathbf{q} f(\mathbf{q}) v(\mathbf{q})$ in Σ_c , as the scheme can straightforwardly account for integration of arbitrary potentials in regions $R_{\mathbf{q}+\mathbf{G}}$ with arbitrary boundaries. Moreover, with the MC averaging scheme, the analytical behavior of $W(\mathbf{q} \rightarrow 0)$ is also appropriately adjusted depending on whether the system behaves like a metal,

semiconductor, or displays a graphene-like linearly vanishing density of states; it is also adjusted based on the dimensionality of the system, as discussed in Ref. 27. These stochastic integration methods have shown success in accurately computing the Coulomb singularity and in improving the convergence of Σ with respect to k-point sampling.^{27,28} To facilitate a complete comparison, we also implemented the MC averaging method into ABINIT for the present work, as will be discussed below.

Aside from the physical model employed for the dielectric matrix and the treatment of the Coulomb divergence, we emphasize that several parameters must be converged in order to achieve meaningful GW results. Both the calculation of ϵ and Σ_c involve unrestricted sums over bands that are truncated up to $N_{\text{eps.}}$ and $N_{\text{sig.}}$, respectively. Additionally, the codes discussed here use plane-wave basis sets; the number of plane-wave basis functions, N_{PW} , used to evaluate ϵ and Σ , is expanded up to an energy-cutoff ϵ_{cut} . These three parameters $N_{\text{eps.}}$, $N_{\text{sig.}}$, and N_{PW} are interdependent, and their convergence needs to be addressed simultaneously.^{9,12} Here, we extrapolate the GW QP gaps (energy eigenvalue differences) to the complete basis set (CBS) limit with a function of the form³⁴

$$f(N_{\text{eps.}}, N_{\text{PW}}, N_{\text{sig.}}) = \left(\frac{a_1}{N_{\text{eps.}}} + b_1 \right) \left(\frac{a_2}{N_{\text{PW}}} + b_2 \right) \left(\frac{a_3}{N_{\text{sig.}}} + b_3 \right), \quad (11)$$

where a_1 , a_2 , a_3 , b_1 , b_2 , and b_3 are constants to be determined. Other important convergence parameters and considerations include the k-point sampling of the Brillouin zone, pseudopotential choice, basis used to describe the wavefunctions, and in the case of full-frequency calculations, the frequency sampling on the real and imaginary axis.

III. TECHNICAL DETAILS

In what follows, we compare GW calculations for several materials using three codes implementing the same approaches. For all materials considered, we fix the lattice parameters to the experimental values. These are, for Si in the diamond structure, fcc Au, rutile TiO_2 , and wurtzite ZnO, respectively, 5.43 Å, 4.08 Å, ($a = 4.60$, $c = 2.9$) Å, and ($a = 3.25$, $c = 5.20$) Å. We use norm-conserving Fritz-Haber Institute pseudopotentials with 6, 4, 12 and 20 valence electrons for O, Si, Ti and Zn, respectively. For Au, we use Optimized Norm-Conserving Vanderbilt Pseudopotentials (ONCVP)⁴⁸ with 19 valence electrons. We use a Perdew-Burke-Ernzerhof (PBE)⁴⁹ starting point for GW , except for ZnO in which the Local Density Approximation (LDA) is used for the sake of comparison to previous works. Our DFT calculations use a k-point mesh and a plane-wave energy-cutoff which ensure that the total energies are converged within 50 meV per unit cell. The k-point mesh is consistent with

that for GW calculations, see below; we use a plane-wave energy cutoff to represent wavefunctions of 40, 88, 300 and 300 Ry for silicon, gold, TiO_2 and ZnO , respectively. The GW parameters are carefully set to converge quasiparticle energies to 0.1 eV; for silicon, we use a Γ -centered Monkhorst-Pack grid of $12 \times 12 \times 12$ k-points, $\epsilon_{\text{cut}} = 20$ Ry and 300 unoccupied states; for gold, we use a mesh of $16 \times 16 \times 16$ k-points, $\epsilon_{\text{cut}} = 32$ Ry, and 400 unoccupied states; for rutile TiO_2 , we use a shifted k-grid of $6 \times 6 \times 10$ k-points and the number of unoccupied states and ϵ_{cut} value were extrapolated to the CBS, as detailed in the supplemental materials (SI); and for wurtzite ZnO , we use a shifted k-grid of $8 \times 8 \times 5$ k-points, and the unoccupied states and ϵ_{cut} are also extrapolated to the CBS. We summarize in Table I of the Supplementary Information (SI) all convergence parameters used for tables and figures in this manuscript.

IV. RESULTS AND DISCUSSION

A. Silicon

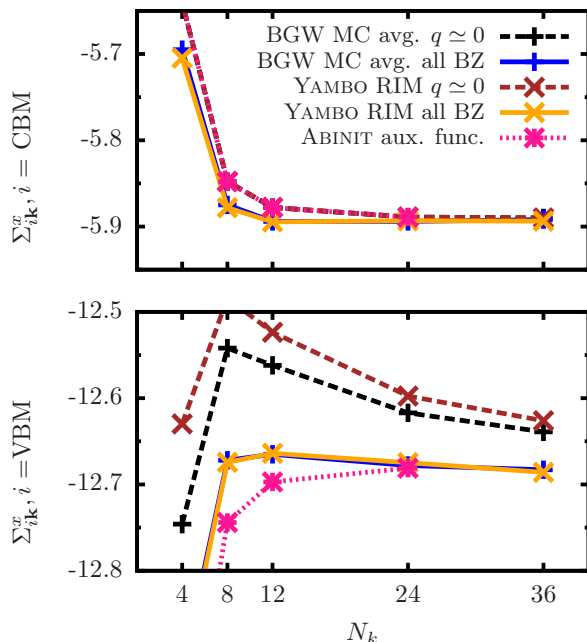


FIG. 1. Convergence of the matrix elements of Σ_x for the VBM and CBM at the Γ point for silicon, with respect to the number of k-points $N_k \times N_k \times N_k$. In the different codes, several techniques are used to treat the Coulomb singularity (see text).

We calculate the GW quasiparticle corrections to the bandstructure of bulk silicon, a typical system for GW calculations. We use a common pseudopotential for all GW calculations, as defined in Section III. The effect of the pseudopotential approximation for silicon is discussed

in Ref. 50.

We first study the accuracy of common approximations to treat the Coulomb divergence, which influences the rate of convergence with respect to k-points. In Fig. 1, we show the convergence of the matrix elements of Σ_x for the valence band maximum (VBM) and conduction band minimum (CBM) at Γ . We consider different techniques to treat the Coulomb singularity, in particular the MC average in BERKELEYGW for only $\mathbf{q} = \mathbf{G} = 0$ (black lines, default up to version 1.1 of BERKELEYGW) and for all \mathbf{G} vectors and q-points in the BZ (blue lines, default starting from version 1.2); the RIM for $q = 0$ only (brown lines) and all BZ (orange line) in YAMBO and the auxiliary-function treatment⁴³ in ABINIT (pink lines). As expected, both the convergence rate with respect to k-points and the converged number of k-points can differ with the choice of method to treat the Coulomb singularity. In this case the RIM and MC average approaches converge fastest, with a grid of $8 \times 8 \times 8$ k-points being sufficient to converge the Σ_x matrix elements for the VBM and CBM within 0.05 eV.

In Table I, we show converged $G_0W_0@PBE$ QP energies for bulk silicon using two different frequency integration schemes and different GW codes. In fact, we find the same QP energies within 0.05 eV for all codes considered here. With respect to the frequency-integration schemes, we find that the PPM in the GN or HL fashions provide a gap for Si within 0.1 eV with respect to the full frequency (FF-CD) reference. Importantly, for a given frequency-integration scheme, the QP energies obtained with the different codes considered here agree within a tolerance better than 0.05 eV, demonstrating that the same GW corrections can be found with different codes.

We highlight that the VBM, CBM, and gap energies calculated with BERKELEYGW and ABINIT with FF-CD agree with the energies obtained with YAMBO and FF-RA. This result serves as a numerical verification of the equivalence between the implemented FF-CD and FF-RA integration schemes, which was demonstrated exactly only for the electron gas.³¹

B. Gold

We now revisit the G_0W_0 corrections to the scalar-relativistic band structure of bulk gold, a relatively difficult case for GW due to convergence issues, the non-negligible influence of semicore orbitals on the band structure, and relativistic effects.^{51,52} In what follows, we neglect spin-orbit interactions. We first converge the number of bands and ϵ_{cut} , as detailed in the SI; 400 unoccupied states and $\epsilon_{\text{cut}} = 32$ Ry ensures a convergence of 0.15 eV in the QP gaps between occupied and unoccupied bands across the Brillouin zone in a relatively large window of energies up to ~ 15 eV above the Fermi level. Secondly, we uniformly increase the k-point mesh up to $16 \times 16 \times 16$. We observe differences in k-point convergence rate that can be traced to the specific

| | QP energies of silicon (eV) | | | | | | | |
|-----|-----------------------------|-------|-------|--------|-------|-------|-------|-------|
| | PPM-GN | | | PPM-HL | | FF-CD | | FF-RA |
| | ABI | BGW | YMB | ABI | BGW | ABI | BGW | YMB |
| VBM | -0.64 | -0.64 | -0.64 | -0.95 | -0.95 | -0.74 | -0.79 | -0.72 |
| CBM | 0.52 | 0.53 | 0.52 | 0.29 | 0.28 | 0.48 | 0.49 | 0.49 |
| Gap | 1.16 | 1.17 | 1.16 | 1.24 | 1.24 | 1.22 | 1.28 | 1.21 |

TABLE I. VBM, CBM and fundamental energy-gap of silicon calculated within GW with several codes using different frequency-integration schemes. Band energies are shown with respect to the DFT VBM.

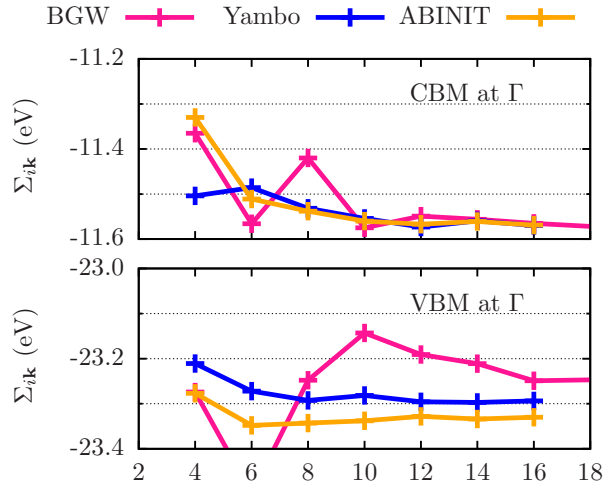


FIG. 2. Convergence of the GW self-energy of gold. We show Σ_{ik} matrix elements for $\mathbf{k} = \Gamma$ and $i = \text{VBM/CBM}$. We consider uniform k -point grids of $N_k \times N_k \times N_k$ k points. The codes used here implement particular sets of approximations to treat metals (see text).

numerical methods used. BERKELEYGW uses a zero-temperature formalism, and a long wavelength limit of the head ($\mathbf{G} = \mathbf{G}' = 0$ component) of the inverse dielectric matrix is $\epsilon_{00}^{-1}(q \rightarrow 0) \sim q^2$ specific to metals. This in turn modifies the MC averaging scheme, since the head of the screened Coulomb potential $W_{00}(\mathbf{q})$ is now a finite and smooth function for $q \rightarrow 0$ ²⁷. On the other hand, ABINIT and YAMBO use finite-temperature occupation factors, requiring a smearing parameter. Here we use Gaussian smearing with a broadening of 0.010 Ry.

In Fig. 2, we show the matrix elements of Σ calculated with sets of k -points of increasing size; here we set $\epsilon_{\text{cut}} = 32$ Ry and $N = 400$. As mentioned, the rate of convergence depends on the treatment of band occupations and the Coulomb singularity. While ABINIT and YAMBO use partial occupations consistent with the underlying DFT code, BERKELEYGW uses a zero-temperature scheme where the bands are either fully-occupied or fully-empty. Moreover, BERKELEYGW uses a particular metal-screening scheme to treat $\epsilon(q \rightarrow 0)$ as described in Ref. 27. With these different approaches, as expected, the self-energy can converge at different rates with respect to the k -point sampling (see Fig. 2). Importantly, when using a relatively-dense mesh of $16 \times 16 \times 16$

k -points, the codes considered here agree within 0.1 eV in the predicted self-energy of the VBM/CBM at Γ , demonstrating that for metals the codes predict the same QP energies when convergence is reached.

In Table II we show that the matrix elements of Σ for bands around the Fermi level calculated with the different codes. The scalar-relativistic DFT band structure and the Brillouin zone are shown in the SI. The GW corrections agree within 0.05 eV, corroborating that at convergence different codes give the same QP energies.

| | GW -PPM self-energy for gold (eV) | | |
|---------------|-------------------------------------|------------|--------|
| | ABINIT | BERKELEYGW | YAMBO |
| Γ_{12} | -23.33 | -23.35 | -23.29 |
| X_5 | -24.25 | -24.20 | -24.20 |
| $X_{4'}$ | -12.98 | -13.08 | -12.97 |

TABLE II. Absolute GW self-energy for gold at high-symmetry k points, obtained from a scalar-relativistic PBE DFT calculation. Calculations were performed with three different codes and with the PPM-GN.

C. Rutile TiO_2

Rutile has been the subject of several GW studies, and the reported G_0W_0 gaps range from 3.1 to 4.8 eV^{11,16–20,24}. Part of the reported disagreement comes from the treatment of the frequency dependence of Σ . As detailed in Ref. 11, the fundamental gap calculated with certain PPMs can deviate considerably (by up to 1.1 eV) from a full-frequency reference. The sensitivity of the TiO_2 gap to the manner in which the frequency dependence of Σ is treated makes rutile an interesting case to investigate the effect and accuracy of PPM and FF methods. As mentioned previously, we use FHI-type pseudopotentials including semicore states consistently in all calculations performed with different codes. Although the choice of pseudopotentials for GW is not studied in this work, we found that our results for rutile are somewhat modified (by less than 0.1 eV) relative to those obtained with other PPs, such as Gaussian⁵³ and pseudo-dojo-v0.2²⁵ PPs (see Appendix A for more details).

We first examine the $G_0W_0@PBE$ QP energies of rutile TiO_2 obtained from different codes, frequency-integration schemes, and in the case of PPMs, choices

| Rutile: (unconverged) QP energies obtained with a spherical-cutoff method (eV) | | | | | | | | | | |
|--|--------|--------|-------|---------|--------|---------|--------|-------|--------|-------|
| | PPM-GN | | | PPM-HL* | | PPM-HL† | | FF-CD | | FF-RA |
| | BGW | ABINIT | YAMBO | BGW | ABINIT | BGW | ABINIT | BGW | ABINIT | YAMBO |
| VBM | 1.66 | 1.66 | 1.66 | 1.53 | 1.58 | 1.27 | 1.32 | 1.59 | 1.59 | 1.59 |
| CBM | 5.47 | 5.47 | 5.47 | 5.62 | 5.58 | 5.98 | 5.94 | 5.45 | 5.45 | 5.43 |
| Gap | 3.81 | 3.81 | 3.81 | 4.09 | 4.00 | 4.71 | 4.62 | 3.86 | 3.86 | 3.84 |

TABLE III. QP energies for rutile within a spherical-cutoff technique. This comparison is performed with small convergence parameters: a $6 \times 6 \times 10$ k-point grid and $\epsilon_{\text{cut}} = 20$ Ry. The actual QP energies of rutile are shown in Table IV. We use different codes and frequency-integration schemes (see text) For PPM-HL, unfulfilled PPM modes ($\omega^{\text{unf.}}$) are either * set to 1 hartree or † neglected.

| Rutile TiO ₂ QP bandgap (eV) | | | | |
|---|-----------|--------|-------|-----------|
| Code | Potential | Freq. | E_g | Ref. |
| YAMBO | NC-PP | PPM-GN | 3.2 | This work |
| ABINIT | NC-PP | PPM-GN | 3.2 | This work |
| BGW | NC-PP | PPM-GN | 3.2 | This work |
| BGW | NC-PP | FF-CD | 3.3 | This work |
| BGW | NC-PP | PPM-HL | 3.1 | 19 |
| TOMBO | AE | PPM-HL | 4.0 | 20, 24 |
| YAMBO | NC-PP | PPM-GN | 3.6 | 17 |
| SAX | NC-PP | PPM-GN | 3.4 | 18 |
| | AE | | 4.8 | 16 |
| YAMBO | NC-PP | FF-CD | 3.3 | 11 |
| TOMBO | AE | FF* | 3.3 | 20, 24 |

TABLE IV. We show the fundamental energy-gap of rutile calculated with G_0W_0 using different set of approximations within different codes, such as the frequency-integration scheme, basis set and pseudopotentials/all-electron. * FF method in the complex plane²⁰.

for $\omega^{\text{unf.}}$, as shown in Table III. The PPM-GN predicts the VBM, CBM, and gap of rutile within 0.1 eV of the FF reference. The accurate performance of the PPM-GN has been observed consistently for other systems, including other transition metal oxides^{10,12,13}.

We now examine the PPM-HL and in particular the effect of the different choices for $\omega^{\text{unf.}}$. Interestingly, when the terms with unfulfilled PPM modes are set to 1-Ha, the PPM-HL yields results within 0.1 eV of the PPM-GN and FF approaches, and when neglecting components with $\omega^{\text{unf.}}$ the results tend to deviate by up to 0.8 eV from the FF reference. This clearly indicates that the performance of PPMs for rutile is highly sensitive to the treatment of unfulfilled PPM modes. For rutile, $\omega^{\text{unf.}}$ make up an alarming proportion of the dielectric function ($\sim 54\%$ of the matrix elements), which suggests the need for a full-frequency treatment of ϵ , in agreement with Ref. 11. The fraction of unfulfilled PPM modes is therefore an important indicator of whether a full frequency approach is required.

We now compare the G_0W_0 self-energy calculated with different codes in Table III. When using the PPM-HL, the self-energy can deviate by up to 0.1 eV for the different codes used here, due to different variants of the PPM-HL being implemented; while ABINIT implements

| ZnO QP energies (unconverged) (eV) | | | | | | |
|------------------------------------|--------|--------|-------|-------|--------|-------|
| | PPM-GN | | | FF-CD | | FF-RA |
| | BGW | ABINIT | YAMBO | BGW | ABINIT | YAMBO |
| VBM | 4.26 | 4.29 | 4.26 | 4.27 | 4.26 | 4.26 |
| CBM | 8.43 | 8.43 | 8.43 | 8.40 | 8.42 | 8.41 |
| Gap | 4.17 | 4.14 | 4.18 | 4.14 | 4.15 | 4.15 |

TABLE V. GW quasiparticle energies of ZnO within a spherical-cutoff technique. The three GW codes, ABINIT, YAMBO and BGW, agree for the calculated QP energies. This comparison is performed with under-converged parameters: a $5 \times 5 \times 4$ k-point grid and $\epsilon_{\text{cut}} = 30$ Ry.

the original version of PPM-HL in Ref. 4, BERKELEYGW uses a modified version of the PPM to deal with non-centrosymmetric systems as detailed in Ref. 27. Assessing these small variations in the PPM is beyond the scope of this work. When using the PPM-GN or FF methods, the agreement is better than 20 meV, similar to the silicon case. Importantly, we find that the quasiparticle energies predicted by the different codes agree within 0.1 eV when using the same treatment of the frequency-dependence.

To converge the GW gap of rutile we extrapolate the interdependent GW parameters (ϵ_{cut} , N_{sig} , and N_{eps}) to the CBS limit, as described above and in the SI. The converged bandgap is 3.3 eV for the different codes used here; this result also agrees with previous full-frequency calculations of Refs. 11, 20, and 24, as reported in Table IV.

D. Wurtzite Zinc Oxide

Historically, ZnO has been a challenging and controversial system for GW . For ZnO, the GW result is strongly affected by the slow convergence of the Σ_c term⁹. Convergence issues are further aggravated when using PPMs¹², although these PPM-related issues may be partially remedied as illustrated in Ref. 23. Here we only show results with FF methods and the PPM-GN (validated against FF references¹²). For more on the PPM approximation for ZnO, we refer the reader to Refs. 12–14, and 23. Other discrepancies in the GW gap

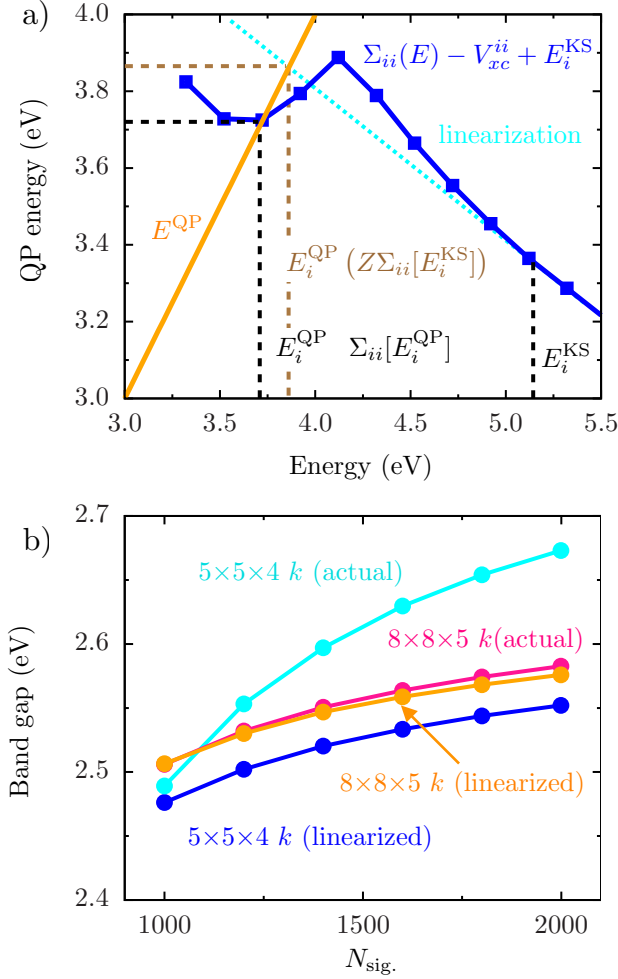


FIG. 3. Linearized vs. actual QP energies for ZnO. a) QP energy for the VBM at the Γ point. We show the actual self-energy, $E_i^{\text{QP}}(\Sigma[E_i^{\text{QP}}])$, and the linearized self-energy evaluated at the KS energy. b) QP bandgap of ZnO. Two shifted k-point grids of $5 \times 5 \times 4$ and $8 \times 8 \times 5$ points are used. The linearized and actual solutions disagree by more than 0.2 eV for the coarser grid, and agree better than 50 meV for the finer grid of $8 \times 8 \times 5$ points. Here we use unconverged GW parameters, as explained in the text.

of ZnO arise from the use of incomplete basis-sets and different pseudopotentials, such as projector-augmented waves¹⁵. Due to these issues, the reported $G_0W_0@LDA$ gaps with different approximations and codes range from 2.3 – 4.5 eV (see Table VI).

We start by showing that the different codes used here agree on the gap of ZnO, for a given pseudopotential. Again, although pseudopotential issues are not discussed here, we find that our results are insensitive (within 0.1 eV) to the choice of PPs tested in this work, as discussed in Appendix A. In Table V, we show unconverged QP energies for ZnO calculated using a spherical-cutoff scheme within $G_0W_0@LDA$. All ZnO results in Table V are computed at the same number of bands, dielec-

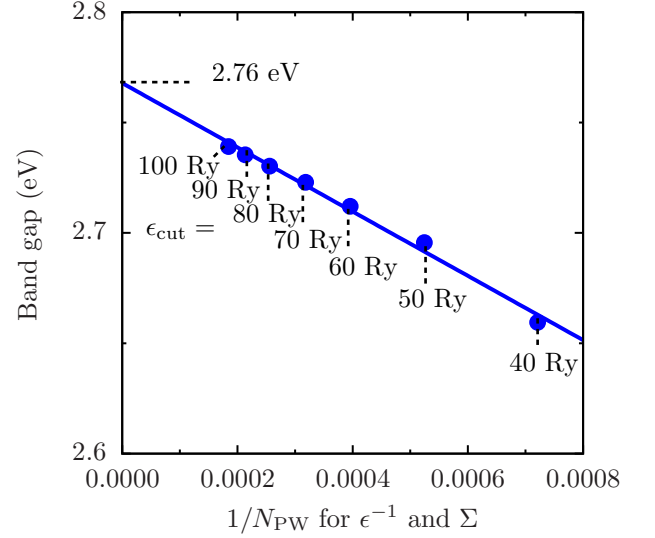


FIG. 4. Convergence of the bandgap of ZnO with respect to the plane-wave basis-set size. The bandgap converges linearly with respect to $1/N_{\text{PW}}$.

| ZnO QP bandgap (eV) | | | | |
|---------------------|-----------|-----------------|-------|-----------|
| Code | Potential | Freq. | E_g | Ref. |
| BGW | NC-PP | PPM-HL | 3.4 | 9 |
| ABINIT | NC-PP | PPM-HL | 3.6 | 12, 13 |
| TOMBO | AE | PPM-HL | 4.5 | 24 |
| ABINIT | NC-PP | PPM-HL | 2.8 | 14 |
| BGW | NC-PP | PPM-HL* | 3.0 | 23 |
| ABINIT | NC-PP | PPM-GN | 2.3 | 12, 13 |
| ABINIT | NC-PP | PPM-GN | 2.6 | 22 |
| | AE | FF ⁺ | 2.4 | 54 |
| ABINIT | NC-PP | FF-CD | 2.4 | 12, 13 |
| VASP | PAW | FF-RA | 2.5 | 55 |
| | AE | FF-CD | 2.8 | 21 |
| VASP | NC-PAW | FF-RA | 2.8 | 15 |
| TOMBO | AE | FF [†] | 2.8 | 24 |
| BGW | NC-PP | FF-CD | 2.8 | This work |

TABLE VI. Fundamental bandgap of ZnO within $G_0W_0@LDA$. The converged gap is extrapolated to the CBS, as detailed in the text. The reported bandgaps using different codes and techniques are shown for comparison. * semicore electrons were excluded to calculate the ground-state density required to fit the PPM-HL parameters, see Ref. 23. † FF integration in the complex plane. + Frequency integration method based on the random-phase approximation^{54,56}.

tric matrix cutoffs, and k-point grid for the purposes of comparison. However, these parameters are underconverged.) We use the GN method, FF-CD method with ABINIT and BERKELEYGW, and the FF-RA method with YAMBO. We set $\epsilon_{\text{cut}} = 30$ Ry, a Coulomb cutoff radius of 19.7177 Bohr, a plasma frequency of 38.82 eV (for PPM-GN), a Γ -centered homogeneous grid of $5 \times 5 \times 4$

k-points and 34 bands, and show that the unconverged GW gap of ZnO calculated with the different codes is consistent within 0.1 eV.

Linearizing the self-energy to the QP energy, especially when using coarse k -grids, can be inaccurate. An illustration of the difference between the linearized and graphically-solved QP energies is given in Fig. 3a. For the VBM, the linearized and graphical solutions can differ by ~ 0.2 eV; for an unconverged set of GW parameters ($5 \times 5 \times 4$ k grid, $\epsilon_{\text{cut}} = 40$ Ry and $N_{\text{eps.}} = N_{\text{sig.}} = 2000$), we find $E_i^{\text{QP}}(\Sigma[E_i^{\text{QP}}]) = 3.7$ eV and $E_i^{\text{QP}}(Z\Sigma[E^{\text{KS}}]) = 3.9$ eV, where $E_i^{\text{KS}} = 5.3$ eV. In Fig. 3b we show the QP bandgap as a function of the number of bands used to evaluate Σ . We use shifted grids of $5 \times 5 \times 4$ and $8 \times 8 \times 5$ k-point grids, $N_{\text{eps.}} = 2000$ and $\epsilon_{\text{cut}} = 40$ Ry. Within the coarser grid the actual (blue dots) and linearized (cyan dots) solutions can disagree by more than 0.1 eV due to features in $\Sigma(\omega)$, as shown in Fig. 3 (a). These features are smoothed out when using a finer grid, reducing the discrepancy associated with linearization.

Having demonstrated good agreement between different codes for ZnO QP energies, we then proceed to converge the gap of ZnO only with BERKELEYGW, excluding the other codes due to our limits on computational resources. To accelerate the convergence with respect to k-points, we use a shifted grid, a common practice well-documented in the past⁵⁷. Using the finest grid of k-points (that is the $8 \times 8 \times 5$ grid), we proceed to converge the $N_{\text{eps.}}$, $N_{\text{sig.}}$ and ϵ_{cut} by extrapolating to the CBS limit (see SI). As shown in Fig. 4, the bandgap converges linearly with respect to N_{PW}^{-1} and a relatively high $\epsilon_{\text{cut}} > 80$ Ry is needed to assure convergence within 0.05 eV. At convergence, we find the $G_0W_0@LDA$ gap of ZnO is 2.8 eV, in agreement with recent calculations, as shown in Table VI.

Finally, we compare our G_0W_0 bandgaps with the corresponding electronic gaps measured in photoemission experiments. Here we use full-frequency G_0W_0 approaches (FF-CD or FF-RA). Note that when comparing to experiment the lattice-renormalization effect should also be included^{58,59}, e.g., the measured/calculated zero-point renormalization (ZPR) of silicon is 62–64 meV, 150 meV for TiO_2 and 156–164 meV for ZnO^{60,61}. Our calculated indirect gap of 1.21–1.28 eV for silicon (without renormalization) is therefore in good agreement with the experimental gap of 1.17 eV⁶². Our result is also in agreement with the seminal work of Ref. 4. As mentioned above, since we neglect spin-orbit effects in this work, we do not compare the GW bandstructure of gold to experiment. Our calculated gap of 3.3 eV of rutile TiO_2 is also in good agreement with the experimental gap of 3.3 ± 0.5 eV^{63,64}. On the other hand, our GW gap of ZnO of 2.8 eV substantially underestimates the reported experimental gap of ~ 3.6 eV^{65,66}. This well-known shortcoming of standard G_0W_0 for ZnO is due to a deficient LDA starting point⁵⁵, and indicates the need for a more accurate starting point or self-consistent schemes. This work reaches a consensus on the value of the G_0W_0

band-gaps of prototype systems, and hence facilitates future work studying beyond-standard GW schemes to improve the accuracy of GW when using a poor mean-field starting point.

V. CONCLUSIONS

In this work, we have revisited the GW approximation for prototype systems with three representative plane-wave-based codes: YAMBO, ABINIT and BERKELEYGW. Within certain choices of approximations and a given set pseudopotentials, the converged GW QP energies calculated with the different codes agree within 0.1 eV, addressing long-standing controversies on the GW results for difficult systems such as ZnO and rutile.

More specifically, we have studied the validity of approximations within one-shot G_0W_0 which can give rise to disagreement in GW results between different codes, in particular the treatment of the Coulomb divergence, convergence, plasmon-pole model approximations, and scheme for capturing the full frequency dependence of Σ . We have benchmarked different techniques to treat the Coulomb divergence, and identified several effective techniques, in particular an auxiliary-function method used in ABINIT, the RIM in YAMBO and the MC average in BERKELEYGW. The latter was implemented in ABINIT in this work. We have provided new insights into the details of PPMs and their effect on GW results, such as the treatment of unfulfilled PPM modes, which for some systems can lead to large deviations (> 0.5 eV) from FF references. We have shown that specific PPM techniques, when treated at the same level in the different codes, provide results in complete agreement independently of the code. Beyond the PPM approximation we have also shown that the FF-CD method implemented in BERKELEYGW provides results in agreement with FF implementations in ABINIT and YAMBO. We highlight that QP energies predicted with the FF-CD method (in the complex plane) agree quantitatively with real-axis FF references, a numerical proof of the validity of the FF-CD.

In summary, our work provides a framework for users and developers to validate and document the precision of new applications and methodological improvements relating to GW codes.

VI. ACKNOWLEDGMENTS

This work was supported by the Center for Computational Study of Excited State Phenomena in Energy Materials at the Lawrence Berkeley National Laboratory, which is funded by the U.S. Department of Energy, Office of Science, Basic Energy Sciences, Materials Sciences and Engineering Division under Contract No. DE-AC02-05CH11231, as part of the Computational Materials Sciences Program. This work is also supported by

the Molecular Foundry through the U.S. Department of Energy, Office of Basic Energy Sciences under the same contract number. We acknowledge the use of computational resources at the National Energy Research Scientific Computing Center (NERSC). We also acknowledge the use of HPC resources from GENCI-CCRT-TGCC (Grants No. 2014-096018). F.B. acknowledges the Enhanced Eurotalent program and the France Berkeley Fund for supporting his sabbatical leave in UC Berkeley. D.V., A.F. and A.M. acknowledge support from European Union H2020-INFRAEDI-2018-1 programme under grant agreement No. 824143 project “MaX - materials at the exascale”. AM acknowledges support from European Union H2020-INFRAIA-2015-1 programme under grant agreement No. 676598 project “Nanoscience Foundries and Fine Analysis - Europe”. O.K.O. and D.O’R. acknowledge the support of Trinity College Dublin’s Studentship Award and School of Physics. Their work was supported by TCHPC (Research IT, Trinity College Dublin), where calculations were performed on the Lonsdale cluster funded through grants from Science Foundation Ireland, and on the Kelvin cluster funded through grants from the Irish Higher Education Authority through its PRTL program. D.V. and A.F. acknowledge PRACE for awarding access to resource Marconi based in Italy at CINECA. M.J.v.S. and G.-M.R. are grateful to F.R.S.-FNRS for financial support through the PDR Grants T.1031.14 (HiT4FiT). They also thank the CÉCI facilities funded by F.R.S.-FNRS (Grant No. 2.5020.1) and Tier-1 supercomputer of the Fédération Wallonie-Bruxelles funded by the Walloon Region (Grant No. 1117545).

Appendix A: The choice of pseudopotential for GW

In this appendix, we study the variation of the bandgap with respect to the *choice of pseudopotential* for TiO_2 and ZnO . We emphasize that the validation of pseudopotentials for GW requires all-electron references and is beyond the scope of the present manuscript. In Table VII we show the G_0W_0 direct gap of rutile calculated with different choices of pseudopotentials. We use a DFT-PBE starting point from ABINIT and consider norm-conserving PPs of the Fritz Haber Institute (FHI)⁶⁸, Optimized Norm-Conserving Vanderbilt (ONCV)⁴⁸ and Hartwigsen-Goedecker-Hutter (HGH)⁵³ kinds. The configuration of choice for Ti is $[\text{Ne}]3s^23p^63d^24s^2$ (including semicore states), and $[\text{He}]2s^22p^6$ for O. We only use PPs available in the literature (see Table VII). Note that the HGH and PD PPs contain non-local core corrections (NLCC), which are subtracted from Σ when calculating the QP energies. In the table, we show the en-

ergy cutoff required to converge the DFT total energy per atom to 0.01 eV and the PP radii, which can be taken as a measure of the PP “hardness”. Here we use BERKELEYGW to compute the G_0W_0 direct gap of rutile using a set of under-converge parameters for GW : $N_{\text{eps.}} = N_{\text{sig.}} = 2000$, $\epsilon_{\text{cut}} = 20$ Ry, the MC avg. technique and a Γ -centered homogeneous grid of $6 \times 6 \times 10$ k-points. Importantly, the GW gaps corresponding to different PP types agree within 0.1 eV, indicating a small dependence of the gap of rutile with the choice of PPs used here.

We now study the sensitiveness of the GW results with respect to the choice of pseudopotential for ZnO . In Table VIII we show the QP gap of ZnO calculated with $G_0W_0@LDA$ using different PPs. The configuration of choice for Zn is $[\text{Ne}]3s^23p^63d^{10}4s^2$ (including semicore states), and $[\text{He}]2s^22p^6$ for O. As in the TiO_2 case, some of the HGH and PSP8 PPs considered here contain NLCCs. We also show the minimum kinetic energy cutoff for the plane-wave expansion to converge the DFT gap within 0.05 eV, and the corresponding DFT-LDA and GW gaps. Here we use BERKELEYGW, the FF-CD method with 20 imaginary frequencies, an uniform sampling of real frequencies spaced by 0.25 eV from 0 to 6 eV, the modified static-reminder method of Ref. 72 and unconverged GW parameters: $\epsilon_{\text{cut}} = 30$ Ry, $N_{\text{sig.}} = N_{\text{eps.}} = 500$. For ZnO the GW and DFT gaps change little, by up to 0.14 and 0.1 eV respectively, with the different choices of PPs. Therefore, the results for ZnO and TiO_2 presented in this manuscript are negligibly affected by the choice of PPs.

| Pseudopotentials for TiO_2 | | | | | |
|-------------------------------------|---|------------------------|--------------|---------------|--|
| PP type | PP radii (Bohr) | $E_{\text{cut.}}$ (Ry) | DFT gap (eV) | GW gap (eV) | |
| FHI ^a | Ti: s 1.48, p 1.62, d 1.70 | 60 | 1.78 | 3.12 | |
| HGH ^b | Ti: s 0.34, p 0.24, d 0.24 O: s 0.22, p 0.21 | 280 | 1.88 | 3.23 | |
| PD ^c | Ti: s 1.35, p 1.30, d 1.65 O: s 1.25, p 1.35 | 60 | 1.88 | 3.23 | |

^a FHI PPs: Ti is defined in the OPIUM-v3.8 user guide⁶⁷ and O is from the FHI98 library^{68,69}.

^b HGH PPs from Refs. 53 and 69.

^c PD PPs from pseudo-dojo-v.2^{25,70}.

TABLE VII. Testing norm-conserving pseudopotentials for rutile. For each PP type we show the radii per angular momentum (s, p or d), the plane-wave energy-cutoff ($E_{\text{cut.}}$) (see text), and the corresponding DFT and GW gap of rutile. We use G_0W_0 PPM-GN with a DFT-PBE starting point, at unconverged GW parameters (see text).

| Pseudopotentials for ZnO | | | | |
|--------------------------|---|-----------------------|--------------|-------------|
| PP type | PP radii (Bohr) | E_{cut} (Ry) | DFT gap (eV) | GW gap (eV) |
| FHI ^a | Zn: s 0.80, p 0.80, d 0.80 O: s 1.20, p 1.20 | 300 | 0.67 | 2.76 |
| RRKJ ^b | Zn: s 1.00, p 1.00, d 0.85 O: s 1.10, p 1.10 | 300 | 0.73 | 2.87 |
| HGH ^c | Zn: s 0.40, p 0.53, d 0.25 O: s 0.22, p 0.21 | 300 | 0.73 | 2.90 |
| PD ^d | Zn: s 1.35, p 1.65, d 1.85 O: s 1.25, p 1.35 | 60 | 0.78 | 2.82 |
| PD ^e | Zn: s 0.80, p 0.80, d 0.60 O: s 0.80, p 0.80 | 500 | 0.74 | 2.84 |

^a FHI PPs from Ref. 12.

^b RRKJ⁷¹ PPs from Ref. 23.

^c HGH PPs from Refs. 53 and 69.

^d PD PPs from pseudo-dojo-v.2^{25,70}.

^e PD PPs generated with the ONCVP code⁴⁸.

TABLE VIII. Sensitiveness of the GW gap of ZnO with respect to the choice of PPs. Same as TiO_2 in Table VII. We use G_0W_0 FF-CD with a DFT-LDA starting point at unconverged GW parameters (see text). Note that the GW gaps of ZnO shown in this table agree with the converged gap (= 2.8 eV) due to spurious cancellation of errors.

* trangel@lbl.gov

† jboneaton@lbl.gov

¹ L. Hedin, Phys. Rev. **139**, A796 (1965).

² A. Seidl, A. Görling, P. Vogl, J. A. Majewski, and M. Levy, Phys. Rev. B **53**, 3764 (1996).

³ M. S. Hybertsen and S. G. Louie, Phys. Rev. Lett. **55**, 1418 (1985).

⁴ M. S. Hybertsen and S. G. Louie, Phys. Rev. B **34**, 5390 (1986).

⁵ F. Aryasetiawan and O. Gunnarsson, Rep. Prog. Phys. **61**, 237 (1998).

⁶ W. G. Aulbur, L. Jönsson, and J. W. Wilkins, in *Solid State Physics*, Vol. 54, edited by H. E. a. F. Spaepen (Academic Press, 2000) pp. 1–218.

⁷ G. Onida, L. Reining, and A. Rubio, Rev. Mod. Phys. **74**, 601 (2002).

⁸ S. G. Louie, in *Contemporary Concepts of Condensed Matter Science*, Vol. 2, edited by S. G. L. a. M. L. Cohen (Elsevier, 2006) pp. 9–53.

⁹ B.-C. Shih, Y. Xue, P. Zhang, M. L. Cohen, and S. G. Louie, Phys. Rev. Lett. **105**, 146401 (2010).

¹⁰ R. Shaltaf, G.-M. Rignanese, X. Gonze, F. Giustino, and A. Pasquarello, Phys. Rev. Lett. **100**, 186401 (2008).

¹¹ W. Kang and M. S. Hybertsen, Phys. Rev. B **82**, 085203 (2010).

¹² M. Stankovski, G. Antonius, D. Waroquiers, A. Miglio,

H. Dixit, K. Sankaran, M. Giantomassi, X. Gonze, M. Côté, and G.-M. Rignanese, Phys. Rev. B **84**, 241201 (2011).

¹³ A. Miglio, D. Waroquiers, G. Antonius, M. Giantomassi, M. Stankovski, M. Côté, X. Gonze, and G.-M. Rignanese, Eur. Phys. J. B **85**, 1 (2012).

¹⁴ P. Larson, M. Dvorak, and Z. Wu, Phys. Rev. B **88**, 125205 (2013).

¹⁵ J. Klimeš, M. Kaltak, and G. Kresse, Phys. Rev. B **90**, 075125 (2014).

¹⁶ M. Oshikiri, M. Boero, J. Ye, F. Aryasetiawan, and G. Kido, Thin Solid Films **445**, 168 (2003).

¹⁷ L. Chiodo, J. M. García-Lastra, A. Iacomino, S. Ossicini, J. Zhao, H. Petek, and A. Rubio, Phys. Rev. B **82**, 045207 (2010).

¹⁸ C. E. Patrick and F. Giustino, J. Phys.: Condens. Matter **24**, 202201 (2012).

¹⁹ A. Malashevich, M. Jain, and S. G. Louie, Phys. Rev. B **89**, 075205 (2014).

²⁰ M. Zhang, S. Ono, and K. Ohno, Phys. Rev. B **92** (2015), 10.1103/PhysRevB.92.035205.

²¹ C. Friedrich, M. C. Müller, and S. Blügel, Phys. Rev. B **83**, 081101 (2011); Phys. Rev. B **84**, 039906 (2011).

²² J. A. Berger, L. Reining, and F. s. Sottile, Phys. Rev. B **85**, 085126 (2012).

²³ G. Samsonidze, C.-H. Park, and B. Kozinsky, J. Phys.

- Condens. Matter **26**, 475501 (2014).
- ²⁴ M. Zhang, S. Ono, N. Nagatsuka, and K. Ohno, Phys. Rev. B **93**, 155116 (2016).
- ²⁵ <http://www.pseudo-dojo.org>.
- ²⁶ X. Gonze, F. Jollet, F. A. Araujo, D. Adams, B. Amadon, T. Applencourt, C. Audouze, J.-M. Beuken, J. Bieder, A. Bokhanchuk, E. Bousquet, F. Bruneval, D. Caliste, M. Côté, F. Dahm, F. D. Pieve, M. Delaveau, M. D. Genaro, B. Dorado, C. Espejo, G. Geneste, L. Genovese, A. Gerossier, M. Giantomassi, Y. Gillet, D. Hamann, L. He, G. Jomard, J. L. Janssen, S. L. Roux, A. Levitt, A. Lherbier, F. Liu, I. Lukačević, A. Martin, C. Martins, M. Oliveira, S. Poncé, Y. Pouillon, T. Rangel, G.-M. Rignanese, A. Romero, B. Rousseau, O. Rubel, A. Shukri, M. Stankovski, M. Torrent, M. V. Setten, B. V. Troeye, M. Verstraete, D. Waroquiers, J. Wiktor, B. Xu, A. Zhou, and J. Zwanziger, Computer Physics Communications **205**, 106 (2016).
- ²⁷ J. Deslippe, G. Samsonidze, D. A. Strubbe, M. Jain, M. L. Cohen, and S. G. Louie, Comput. Phys. Commun. **183**, 1269 (2012).
- ²⁸ A. Marini, C. Hogan, M. Grüning, and D. Varsano, Comput. Phys. Commun. **180**, 1392 (2009).
- ²⁹ R. W. Godby and R. J. Needs, Phys. Rev. Lett. **62**, 1169 (1989).
- ³⁰ S. B. Zhang, D. Tománek, M. L. Cohen, S. G. Louie, and M. S. Hybertsen, Phys. Rev. B **40**, 3162 (1989).
- ³¹ B. I. Lundqvist, Phys. kondens. Mater. **7**, 117 (1968).
- ³² M. Giantomassi, M. Stankovski, R. Shaltaf, M. Grüning, F. Bruneval, P. Rinke, and G.-M. Rignanese, phys. stat. sol. (b) **248**, 275 (2011).
- ³³ M. Del Ben, F. H. da Jornada, A. Canning, N. Wichmann, K. Raman, R. Sasanka, C. Yang, S. G. Louie, and J. Deslippe, Comput. Phys. Commun. **235**, 187 (2019).
- ³⁴ M. Del Ben, F. H. da Jornada, G. Antonius, T. Rangel, S. G. Louie, J. Deslippe, and A. Canning, Phys. Rev. B (in press) (2019).
- ³⁵ M. Shishkin and G. Kresse, Phys. Rev. B **74**, 035101 (2006).
- ³⁶ F. Liu, L. Lin, D. Vigil-Fowler, J. Lischner, A. F. Kemper, S. Sharifzadeh, F. H. da Jornada, J. Deslippe, C. Yang, J. B. Neaton, and S. G. Louie, J. Comput. Phys. **286**, 1 (2015).
- ³⁷ Bruneval, *Exchange and Correlation in the Electronic Structure of Solids, from Silicon to Cuprous Oxide: GW Approximation and beyond*, Ph.D. thesis, Ecole Polytechnique, France (2005).
- ³⁸ M. S. Hybertsen and S. G. Louie, Phys. Rev. B **35**, 5585 (1987).
- ³⁹ S. Baroni and R. Resta, Phys. Rev. B **33**, 7017 (1986).
- ⁴⁰ F. Gygi and A. Baldereschi, Phys. Rev. B **34**, 4405 (1986).
- ⁴¹ R. M. Pick, M. H. Cohen, and R. M. Martin, Phys. Rev. B **1**, 910 (1970).
- ⁴² S. Massidda, M. Posternak, and A. Baldereschi, Phys. Rev. B **48**, 5058 (1993).
- ⁴³ P. Carrier, S. Rohra, and A. Görling, Phys. Rev. B **75**, 205126 (2007).
- ⁴⁴ J. Spencer and A. Alavi, Phys. Rev. B **77**, 193110 (2008).
- ⁴⁵ C. A. Rozzi, D. Varsano, A. Marini, E. K. Gross, and A. Rubio, Physical Review B **73**, 205119 (2006).
- ⁴⁶ S. Ismail-Beigi, Physical Review B **73**, 233103 (2006).
- ⁴⁷ O. Pulci, G. Onida, R. Del Sole, and L. Reining, Phys. Rev. Lett. **81**, 5374 (1998).
- ⁴⁸ D. R. Hamann, Phys. Rev. B **88**, 085117 (2013).
- ⁴⁹ J. P. Perdew, K. Burke, and M. Ernzerhof, Phys. Rev. Lett. **77**, 3865 (1996).
- ⁵⁰ R. Gómez-Abal, X. Li, M. Scheffler, and C. Ambrosch-Draxl, Phys. Rev. Lett. **101**, 106404 (2008).
- ⁵¹ T. Rangel, D. Kecik, P. E. Trevisanutto, G.-M. Rignanese, H. Van Swygenhoven, and V. Olevano, Phys. Rev. B **86**, 125125 (2012).
- ⁵² M. Bernardi, J. Mustafa, J. B. Neaton, and S. G. Louie, Nat. Commun. **6**, 7044 (2015).
- ⁵³ C. Hartwigsen, S. Goedecker, and J. Hutter, Phys. Rev. B **58**, 3641 (1998).
- ⁵⁴ M. Usuda, N. Hamada, T. Kotani, and M. van Schilf-gaarde, Phys. Rev. B **66**, 125101 (2002).
- ⁵⁵ L. Y. Lim, S. Lany, Y. J. Chang, E. Rotenberg, A. Zunger, and M. F. Toney, Phys. Rev. B **86**, 235113 (2012).
- ⁵⁶ V. I. Anisimov, *Strong Coulomb Correlations in Electronic Structure Calculations* (CRC Press, 2000) Frequency integration method by F. Ayasetiawan.
- ⁵⁷ F. Sottile, V. Olevano, and L. Reining, Phys. Rev. Lett. **91**, 056402 (2003).
- ⁵⁸ S. Botti and M. A. L. Marques, Phys. Rev. Lett. **110**, 226404 (2013).
- ⁵⁹ G. Antonius, S. Poncé, P. Boulanger, M. Côté, and X. Gonze, Physical Review Letters **112**, 215501 (2014).
- ⁶⁰ M. Cardona and M. L. W. Thewalt, Rev. Mod. Phys. **77**, 1173 (2005).
- ⁶¹ B. Monserrat, Phys. Rev. B **93**, 100301 (2016).
- ⁶² C. Kittel, *Introduction to Solid State Physics*, 6th ed. (John Wiley & Sons, Inc., New York, 1986).
- ⁶³ Y. Tezuka, S. Shin, T. Ishii, T. Ejima, S. Suzuki, and S. Sato, J. Phys. Soc. Jpn. **63**, 347 (1994).
- ⁶⁴ A. K. See and R. A. Bartynski, Phys. Rev. B **50**, 12064 (1994).
- ⁶⁵ S. Tsoi, X. Lu, A. K. Ramdas, H. Alawadhi, M. Grimsditch, M. Cardona, and R. Lauck, Phys. Rev. B **74**, 165203 (2006).
- ⁶⁶ H. Alawadhi, S. Tsoi, X. Lu, A. K. Ramdas, M. Grimsditch, M. Cardona, and R. Lauck, Phys. Rev. B **75**, 205207 (2007).
- ⁶⁷ <http://opium.sourceforge.net>.
- ⁶⁸ M. Fuchs and M. Scheffler, Comput. Phys. Commun. **119**, 67 (1999).
- ⁶⁹ <http://www.abinit.org>.
- ⁷⁰ M. van Setten, M. Giantomassi, E. Bousquet, M. Verstraete, D. Hamann, X. Gonze, and G.-M. Rignanese, Comput. Phys. Commun. **226**, 39 (2018).
- ⁷¹ A. M. Rappe, K. M. Rabe, E. Kaxiras, and J. D. Joannopoulos, Phys. Rev. B **41**, 1227 (1990).
- ⁷² J. Deslippe, G. Samsonidze, M. Jain, M. L. Cohen, and S. G. Louie, Phys. Rev. B **87**, 165124 (2013).

Supplemental Information for “Reproducibility in the G_0W_0 Calculations for Solids”

Tonatiuh Rangel,^{1,2,*} Mauro Del Ben,³ Daniele Varsano,^{4,5} Gabriel Antonius,^{2,6,7}
 Fabien Bruneval,^{8,1,6} Felipe H. da Jornada,^{2,6} Michiel J. van Setten,^{9,5,10} Okan K.
 Orhan,¹¹ David D. O’Regan,¹¹ Andrew Canning,³ Andrea Ferretti,^{4,5} Andrea Marini,^{12,5}
 Gian-Marco Rignanese,^{9,5} Jack Deslippe,¹³ Steven G. Louie,^{2,6} and Jeffrey B. Neaton^{1,2,14}

¹*Molecular Foundry, Lawrence Berkeley National Laboratory, Berkeley, California 94720, United States*

²*Department of Physics, University of California at Berkeley, California 94720, United States*

³*Computational Research Division, Lawrence Berkeley National Laboratory, Berkeley, California, 94720, United States*

⁴*Centro S3, CNR-Istituto Nanoscienze, I-41125 Modena, Italy*

⁵*European Theoretical Spectroscopy Facility (ETSF)*

⁶*Materials Sciences Division, Lawrence Berkeley National Laboratory, Berkeley, California 94720, United States*

⁷*Département de Chimie, Biochimie et Physique, Institut de recherche sur l’hydrogène,
 Université du Québec à Trois-Rivières, Qc, Canada*

⁸*DEN, Service de Recherches de Métallurgie Physique,
 Université Paris-Saclay, CEA, F-91191 Gif-sur-Yvette, France*

⁹*Institute of Condensed Matter and Nanoscience (IMCN),
 Université catholique de Louvain, 1348 Louvain-la-Neuve, Belgium*

¹⁰*IMEC, Kapeldreef 75, 3001 Leuven, Belgium*

¹¹*School of Physics, Trinity College Dublin, The University of Dublin, Dublin 2, Ireland*

¹²*Istituto di Struttura della Materia of the National Research Council,
 Via Salaria Km 29.3, I-00016 Montelibretti, Italy*

¹³*NERSC, Lawrence Berkeley National Laboratory, Berkeley, California 94720, United States*

¹⁴*Kavli Energy Nanosciences Institute at Berkeley, Berkeley, California 94720, United States*

In this Supplemental Information we show convergence studies on the QP energies of silicon, gold, TiO₂ and zinc oxide. We show the technical parameters used in our GW calculations. We describe a simple strategy to compare the results from different GW codes. Finally, we study the sensitiveness of the GW gaps to the choice of pseudopotential.

I. TECHNICAL DETAILS

In Table I we summarize all parameters used in our GW calculations for Tables and Figures in the main manuscript.

II. STRATEGY TO VALIDATE CODES

Comparing the numerical accuracy of different GW codes is a complex task due to the various approximations used in the practice, such as the degree of convergence, the treatment of the Coulomb singularity and frequency dependence of $\Sigma(\omega)$ and the choice of pseudopotentials. Nevertheless, we can isolate the different sources of discrepancy following a *simple strategy*:

1. We start with exactly the same DFT input (wavefunctions and eigenvalues).
2. We avoid the Coulomb singularity by using the spherical-cutoff scheme; and we use the same frequency integration scheme, number of bands, and k -points in BZ integrations.
3. We explore k -point convergence, which is sensitive to the method used to treat the Coulomb singularity (see above).
4. We converge ϵ_{cut} simultaneously with the number

of bands used to evaluate ϵ and Σ ($N_{\text{eps.}}$ and $N_{\text{sig.}}$ respectively).

Below, we describe in more detail our application of this strategy to validate GW codes for bulk crystalline Si, Au, TiO₂, and ZnO.

In TABLE II, we show the GW corrections to the valence band maximum (VBM) and conduction band minimum (CBM) at the Γ point for bulk silicon. We show the corrections calculated with/without the spherical-cutoff technique and using the three different codes used here ABINIT, BERKELEYGW and YAMBO. We set $\epsilon_{\text{cut}} = 20$ Ry, a grid of $4 \times 4 \times 4$ k -points and 10 empty states; with these settings, the GW corrections are underconverged but the level of accuracy is the same for the different codes, facilitating quantitative comparison. When using the spherical-cutoff technique (see last two columns in TABLE II), we obtain the same QP energies with different codes. This result shows that by disentangling the sources of discrepancy with our simple strategy, we can effectively compare output of different GW codes.

III. GOLD

Bulk gold is a more complex case for GW due to approximations to the metal dielectric and the partial band occupations at the Fermi energy. As mentioned in the manuscript, we study the GW corrections to the scalar

| k -point grid | ϵ_{cut} | $N_{\text{eps.}}$ | $N_{\text{sig.}}$ | PP | St. point | Sph. cut. | Ω_p |
|---|--|-------------------|-------------------|------------------|-----------|-----------|------------|
| <i>Silicon</i> | | | | | | | |
| Table I of main manuscript $12 \times 12 \times 12$, unshifted | 40 Ry | 300 | 300 | FHI ^a | PBE | No | 16.60 eV |
| Fig. 1 of main manuscript $4 \times 4 \times 4$, unshifted | 20 Ry | | 4 | FHI ^a | PBE | Yes | 16.60 eV |
| <i>Gold</i> | | | | | | | |
| Table II of main manuscript $16 \times 16 \times 16$, unshifted | 32 Ry | 400 | 400 | PD ^b | PBE | No | 38.88 eV |
| <i>Rutile</i> | | | | | | | |
| Table III of main manuscript $6 \times 6 \times 10$, unshifted | 20 Ry | 100 | 100 | FHI ^c | PBE | Yes | 32.56 eV |
| Table IV of main manuscript $6 \times 6 \times 10$, unshifted | extrapolated to CBS limit ^d | | | FHI ^c | PBE | No | 32.56 eV |
| <i>Zinc Oxide</i> | | | | | | | |
| Table V of main manuscript $5 \times 5 \times 4$, unshifted | 30 Ry | 34 | 34 | FHI ^e | LDA | Yes | 38.82 eV |
| Fig. 3a of main manuscript $5 \times 5 \times 4$ | 40 Ry | 2000 | 2000 | FHI ^e | LDA | No | |
| Fig. 3b of main manuscript Several grids ^{f,g} | 40 Ry | 2000 | 2000 | FHI ^e | LDA | No | |
| Fig. 4 of main manuscript $8 \times 8 \times 5$, shifted ^g | extrapolated to CBS limit ^h | | | FHI ^e | LDA | No | |
| Table VI of main manuscript $8 \times 8 \times 5$, shifted ^g | extrapolated to CBS limit ^h | | | FHI ^e | LDA | No | |

^a FHI98 PP¹ from the ABINIT web site.

^b PD PP from pseudo-dojo-v.2^{2,3}.

^c FHI PPs: Ti is defined in the OPIUM-v3.8 user guide⁴ and O is from the FHI98 library^{1,5}.

^d Number of bands and ϵ_{cut} extrapolated to the complete basis set (CBS) limit, see Section IV.

^e FHI PPs from Ref. 6.

^f Shifted and unshifted grids of $5 \times 5 \times 4$ and $8 \times 8 \times 5$ k -points.

^g Shifted grids are only used calculate the dielectric constant.

^h Extrapolation to the CBS limit, read Section D of main manuscript.

TABLE I. Parameters used in our GW calculations. We report our choice of k -point grid, energy cutoff for the screening (ϵ_{cut}), number of bands used to calculate the dielectric function ($N_{\text{eps.}}$) and the GW self-energy ($N_{\text{sig.}}$), pseudopotential (PP), DFT starting point (St. point), whether a spherical cutoff was used (Sph. cut.). Additionally, a plasma frequency (Ω_p) is shown when referring to PPM-GN calculations.

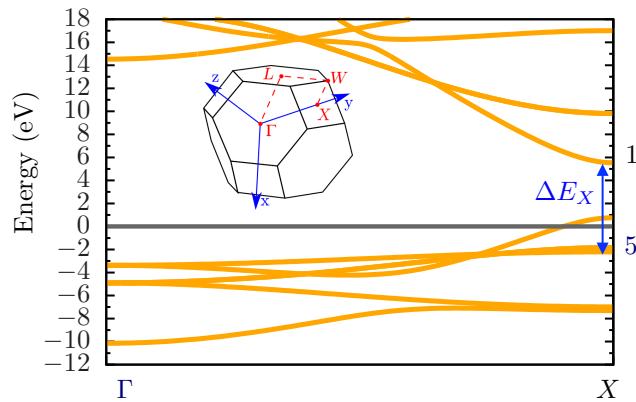


FIG. 1. Scalar-relativistic bandstructure of gold calculated with DFT-PBE. The Brillouin zone is shown as an inset.

relativistic bandstructure of gold, shown in FIG. 1. Notice that this should not be compared to experiment, as

the strong spin-orbit effects are neglected.

We first converge the number of bands and planewaves used for the dielectric function and Σ , using a fixed k -point sampling of $8 \times 8 \times 8$ k -points, the PPM-GN, and the ABINIT code. The linear extrapolation to an infinite number of bands and planewaves is done in a two-step procedure. First, for a fixed ϵ_{cut} , we extrapolate the number of bands N for Σ and ϵ to $N \rightarrow \infty$ (see FIG. 2). Second, the resulting gaps are linearly extrapolated to the complete basis set limit (CBS) (see the inset). The choice of linear extrapolation is motivated by recent work⁷, and here the fit is satisfactory with a standard deviation of < 0.005 eV. We find an extrapolated gap at X ($X_5 \rightarrow X_1$) of 5.59 eV. Setting this gap as the reference, we find that the set of parameters $\epsilon_{\text{cut}} = 32$ Ry and $N = 400$ are sufficient to converge the gap within < 0.1 eV.

| Unconverged GW corrections for silicon at Γ in eV | | | | |
|--|------------|------------|------------------|------------|
| Valence band maximum | | | | |
| | No cutoff | | Spherical cutoff | |
| | Σ_x | Σ_c | Σ_x | Σ_c |
| BERKELEYGW | -12.746 | 2.030 | -13.049 | 0.969 |
| ABINIT | -13.057 | 2.178 | -13.049 | 0.969 |
| YAMBO | -12.630 | 1.975 | -13.050 | 0.969 |
| Conduction band minimum | | | | |
| | No cutoff | | Spherical cutoff | |
| | Σ_x | Σ_c | Σ_x | Σ_c |
| BERKELEYGW | -5.640 | -2.946 | -5.709 | -1.984 |
| ABINIT | -5.640 | -3.094 | -5.709 | -1.984 |
| YAMBO | -5.640 | -2.890 | -5.709 | -1.984 |

TABLE II. GW corrections to the VBM/CBM of silicon with low convergence parameters (read text). The unconverged GW corrections are identical for different codes when using the spherical-cutoff technique (last two columns), illustrating how to cheaply evaluate the numerical accuracy of GW codes.

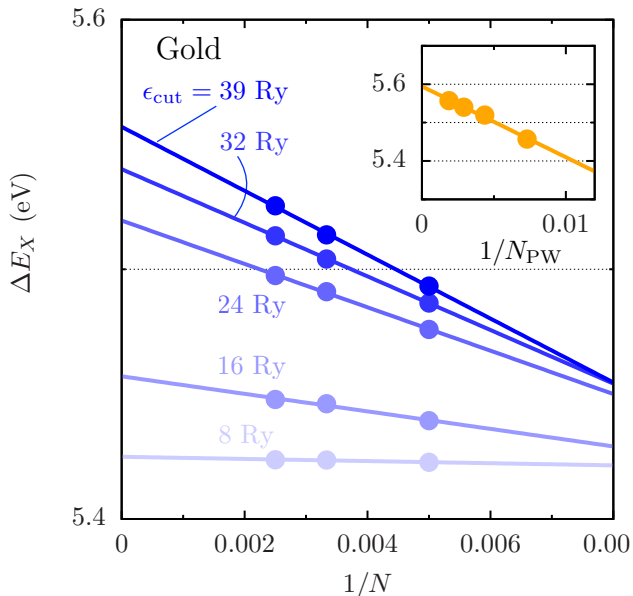


FIG. 2. Energy bandgap ΔE_X , defined in FIG. 1, of gold. The bandgap for different values of ϵ_{cut} and bands N (for both Σ_c and ϵ) is linearly extrapolated to $N \rightarrow \infty$ (blue lines). Inset: the resulting gaps are then extrapolated to the CBS limit ($N_{\text{PW}} \rightarrow \infty$).

IV. TiO_2

For rutile TiO_2 , we first study the convergence of Σ with respect to the number of bands and cutoff used for the GW sums. In FIG. 4, we show $\Sigma_{i\mathbf{k}}^x$ matrix elements as a function of the k -point mesh. Consistent with the silicon case (see main manuscript), some methods, such as the YAMBO analytic method (brown lines) and the BERKELEYGW MC avg. on $q \simeq 0$ (black lines) can exhibit a slow convergence rate. Importantly, with a mesh of $6 \times 6 \times 10$ k -points or denser, when using the RIM (or-

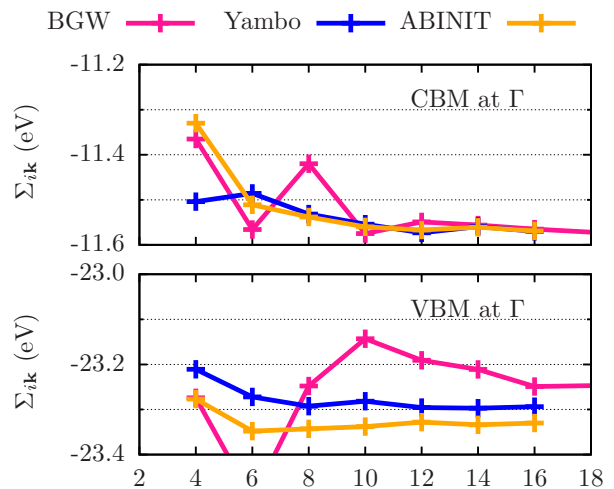


FIG. 3. Convergence of the GW self-energy of gold. We show $\Sigma_{i\mathbf{k}}$ matrix elements for $\mathbf{k} = \Gamma$ and $i = \text{VBM/CBM}$. We consider uniform k -point grids of $N_k \times N_k \times N_k$ k points. The codes used here implement particular sets of approximations to treat metals (read text).

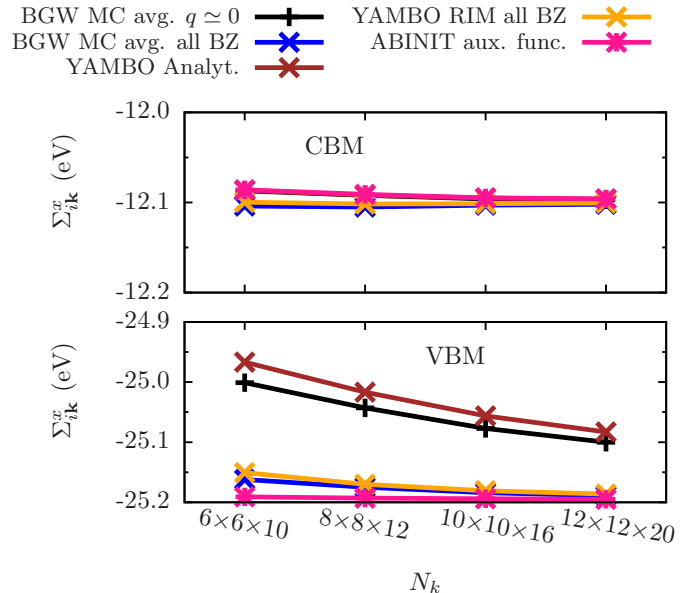


FIG. 4. Convergence of the $\Sigma_{i\mathbf{k}}^x$ matrix elements with respect to the k -point mesh for rutile. Shown are the matrix elements for the Γ point and the VBM/CBM. Several codes and methods are considered (read text).

ange lines) or MC average (blue lines) over the entire BZ, or the auxiliary function of Carrier (pink lines), all codes converge $\Sigma_{i\mathbf{k}}^x$ for the VBM/CBM within < 0.1 eV. Moreover, in TABLE III and IV of the main manuscript, we show that the GW codes used in this work agree within 0.1 eV in the predicted gap of rutile.

We now converge the GW parameters with BERKELEYGW. In FIG. 5, we show the gap of rutile for given values of ϵ_{cut} and $N_{\text{sig.}}$, fixing $N_{\text{eps.}}$ to 2000 (blue dots). For each value of ϵ_{cut} , we linearly extrapolate the gaps

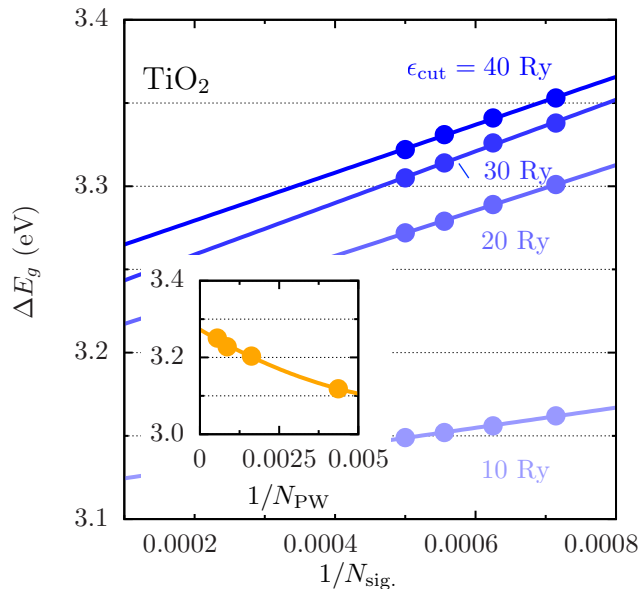


FIG. 5. Fundamental bandgap ΔE_g of rutile. The bandgap for different values of ϵ_{cut} and $N_{\text{sig.}}$ is extrapolated to the limit of an infinite number of bands (blue lines). Here we fix $N_{\text{eps.}} = 2000$. Inset: the resulting gaps are then extrapolated to the limit of an infinite number of plane-waves N_{PW} in the basis set.

with $1/N_{\text{sig.}}$ to $N_{\text{sig.}} \rightarrow \infty$ (blue lines). The resulting gaps are then used to further extrapolate the gap to the CBS limit with $1/N_{\text{PW}}$; a linear extrapolation results in a gap of 3.26 ± 50 meV, and the accuracy is increased with a quadratic extrapolation resulting in $\Delta E_g = 3.27 \pm 10$ meV (see the inset). With this procedure, or alternatively by extrapolating simultaneously the parameters (ϵ_{cut} , $N_{\text{eps.}}$, and $N_{\text{sig.}}$) via Eqn. 7 of the main text,

$$f(N_{\text{eps.}}, N_{\text{PW}}, N_{\text{sig.}}) = \left(\frac{a_1}{N_{\text{eps.}}} + b_1 \right) \left(\frac{a_2}{N_{\text{PW}}} + b_2 \right) \left(\frac{a_3}{N_{\text{sig.}}} + b_3 \right), \quad (1)$$

we obtain a converged *GW* gap of rutile of 3.3 eV.

V. ZnO

We show that the *GW* codes considered here can predict the same QP energies for ZnO within a given choice of PPs and frequency-integration method. In TABLE V of the main manuscript we show the VBM, CBM and fundamental gap of ZnO calculated with different codes and using a spherical-cutoff technique. As our aim is to compare output of different codes, we reduce computational cost and use under-converged *GW* parameters: $\epsilon_{\text{cut}} = 80$ Ry, $5 \times 5 \times 4$ k -points and 34 bands to evaluate Σ . As expected, we find a negligible deviation for the PPM (GN) with respect to FF-integration, in agreement with Refs. 6, 8, and 9. Remarkably, the QP energies obtained with different codes agree within 0.03 eV.

Next, we converge the QP gap of ZnO with BERKELEYGW. Here we use an LDA starting point, a shifted grid of $8 \times 8 \times 5$ k -points for ϵ and Σ , and FF-CD with the same frequency grid as above. We then extrapolate the fundamental gap of ZnO, similar to previous cases. First, we calculate the gap for fixed values of ϵ_{cut} and extrapolating to $N_{\text{sig.}} \rightarrow \infty$ with $1/N_{\text{sig.}}$ (see FIG. 3 of main text); here we set $N_{\text{eps.}} = 2000$. Second, the gap is extrapolated to an infinite basis-set size with $1/N_{\text{PW}}$ (see FIG. 4 of main text). The converged gap of ZnO with this procedure is 2.76 eV. Alternatively, we can extrapolate the *GW* parameters simultaneously via Eqn. 1, where for ZnO we find $a_1 = -19.1213$, $a_2 = -58.4158$, $a_3 = -96.9096$, $b_1 = 1.3356$, $b_2 = 1.4735$ and $b_3 = 1.4127$ (in eV). With this alternative procedure the extrapolated bandgap is $b_1 b_2 b_3 = 2.78$ eV, coinciding with the previously extrapolated gap (with a deviation of only 0.02 eV).

* trangel@lbl.gov

¹ M. Fuchs and M. Scheffler, *Comput. Phys. Commun.* **119**, 67 (1999).

² <http://www.pseudo-dojjo.org>.

³ M. van Setten, M. Giantomassi, E. Bousquet, M. Verstraete, D. Hamann, X. Gonze, and G.-M. Rignanese, *Comput. Phys. Commun.* **226**, 39 (2018).

⁴ <http://opium.sourceforge.net>.

⁵ <http://www.abinit.org>.

⁶ M. Stankovski, G. Antonius, D. Waroquiers, A. Miglio,

H. Dixit, K. Sankaran, M. Giantomassi, X. Gonze, M. Côté, and G.-M. Rignanese, *Phys. Rev. B* **84**, 241201 (2011).

⁷ J. Klimeš, M. Kaltak, and G. Kresse, *Phys. Rev. B* **90**, 075125 (2014).

⁸ A. Miglio, D. Waroquiers, G. Antonius, M. Giantomassi, M. Stankovski, M. Côté, X. Gonze, and G.-M. Rignanese, *Eur. Phys. J. B* **85**, 1 (2012).

⁹ P. Larson, M. Dvorak, and Z. Wu, *Phys. Rev. B* **88**, 125205 (2013).